



Cite this: *Phys. Chem. Chem. Phys.*, 2016, **18**, 30686

Revisiting the zero-temperature phase diagram of stoichiometric SrCoO₃ with first-principles methods†

Pablo Rivero^a and Claudio Cazorla^{*bc}

By using first-principles methods based on density functional theory we revisited the zero-temperature phase diagram of stoichiometric SrCoO₃, a ferromagnetic metallic perovskite that undergoes significant structural, electronic, and magnetic changes as its content of oxygen is decreased. We considered both bulk and epitaxial thin film geometries. In the bulk case, we found that a tetragonal *P4/mbm* phase with moderate Jahn–Teller distortions and a *c/a* ratio of $\sim 1/\sqrt{2}$ is consistently predicted to have a lower energy than the thus far assumed ground-state cubic *Pm $\bar{3}m$* phase. In thin films, we found two phase transitions occurring at compressive and tensile epitaxial strains. However, in contrast to previous theoretical predictions, our results show that: (i) the phase transition induced by tensile strain is isostructural and involves only a change in magnetic spin order (that is, not a metallic to insulator transformation), and (ii) the phase transition induced by compressive strain comprises simultaneous structural, electronic and magnetic spin order changes, but the required epitaxial stress is so large ($< -6\%$) that is unlikely to be observed in practice. Our findings call for a revision of the crystallographic data obtained in fully oxidised SrCoO₃ samples at low temperatures, as well as of previous first-principles studies.

Received 7th September 2016,
Accepted 14th October 2016

DOI: 10.1039/c6cp06191e

www.rsc.org/pccp

1. Introduction

Oxide perovskites with the general formula ABO₃, in which A and B denote different cations, can undergo abrupt structural, magnetic, and electronic changes upon application of small external fields (*e.g.*, electric, magnetic, and mechanical) and variation of temperature.^{1–10} This singular reactivity converts oxide perovskites into excellent candidate materials for developing new information storage and energy conversion technologies. One illustrative example is the design of spintronic devices, in which spin-polarised electric currents are generated with electromagnetic fields or through spin-injection from a ferromagnetic material, in order to exploit the magnetic degree of freedom of electrons.^{11–13} In the latter context, ferromagnetic metallic perovskites appear to be especially valuable as they can be employed directly as electrodes in complex oxide heterostructures.

SrCoO_{*x*} is a ferromagnetic metallic perovskite in which significant structural, electronic, and magnetic order changes occur as its content of oxygen is varied ($2.5 \leq x \leq 3.0$).^{14,15} In stoichiometric samples ($x = 3.0$) the crystalline phase that

has been repeatedly reported as the ground state is the perovskite *Pm $\bar{3}m$* structure, which exhibits ferromagnetic (FM) spin order at temperatures below $T_C = 280\text{--}305$ K.^{16–18} Experiments and theoretical calculations have assuredly shown that SrCoO₃ possesses an intermediate spin (IS) state with a magnetic moment of $\sim 2.6 \mu_B$ per Co ion.^{18–21} In non-stoichiometric samples with a high oxygen deficiency ($x = 2.5$) the system adopts the brownmillerite phase, which presents atomically ordered one-dimensional vacancy channels and antiferromagnetic (A) spin order at temperatures below $T_C = 570$ K.^{22–24}

Recently, it has been shown that the content of oxygen in SrCoO_{*x*} thin films can be effectively tuned by means of epitaxial strain.^{14,15,25–28} This control of oxygen non-stoichiometry offers a promising new route for designing multifunctional oxide materials with improved electrochemical, magnetoresistance, and catalytic properties. Interestingly, Lee and Rabe have identified SrCoO₃ thin films as good candidate materials in which large magnetoelectric effects can be observed, that is, a strong coupling between polar and magnetic degrees of freedom, based on the results of first-principles density functional theory (DFT) calculations.^{29,30} Specifically, it has been predicted that simultaneous magnetic–ferroelectric and metal–insulator transitions could be induced in SrCoO₃ by means of moderate tensile and compressive epitaxial strains. If confirmed, these results could advance the development of low-power high-efficiency electronic and energy conversion technologies.

^a Center for Computation and Technology, Louisiana State University, Baton Rouge, Louisiana 70803, USA

^b School of Materials Science and Engineering, UNSW Australia, Sydney, NSW 2052, Australia. E-mail: c.cazorla@unsw.edu.au

^c Integrated Materials Design Centre, UNSW Australia, Sydney, NSW 2052, Australia

† PACS numbers: 77.55.Nv, 61.50.Ks, 68.65.Cd, 77.80.bn.

Here, we present a revision of the zero-temperature phase diagram of stoichiometric SrCoO₃ (SCO), both in bulk and thin film geometries, using a wide variety of first-principles DFT techniques (*i.e.*, LDA+*U*, GGA+*U* and hybrid exchange–correlation functionals). Our computational analysis consistently shows that, rather than the well-known cubic *Pm* $\bar{3}$ *m* phase, a tetragonal *P4/mbm* phase with moderate Jahn–Teller distortions and a *c/a* ratio of $\sim 1/\sqrt{2}$ is the energetically most favorable phase in bulk SCO at zero temperature. We arrived at the same conclusion also when considering the application of hydrostatic pressures of up to 70 GPa. This central outcome either calls for a revision of previous crystallographic analysis performed in SCO at low temperatures, or it well represents a failure of DFT methods in describing the competition among crystalline phases in this highly correlated material. We have also investigated the energy, magnetic, and electronic properties of SCO thin films in a wide interval of epitaxial strains, $-7\% \leq \eta \leq +5\%$ ($\eta \equiv (a - a_0)/a_0$, where a_0 is the in-plane equilibrium distance between cations of the same species), using computational techniques similar to those employed by Lee and Rabe (*i.e.*, DFT GGA+*U*).^{29,30} Our results show a phase-transition scenario that is compatible with recent experimental observations but appreciably different from the one proposed previously. Actually, our findings lower the expectations of realising large magnetoelectricity in stoichiometric SCO thin films.

The organisation of this article is as follows. In the following section we provide an overview of the computational methods employed in this study. Next, we present our results along with some discussion. Finally, we summarise our main findings in Section IV.

II. Computational methods

In order to accurately describe the physical properties of SrCoO₃, it is necessary to use methods that go beyond standard DFT, *e.g.*, GGA+*U* (or LDA+*U*) and hybrid functionals, due to the presence of strongly correlated d electrons. The GGA+*U* approximation is based on a Hubbard-type Hamiltonian approach in which an on-site constant effective potential is introduced to account for the intra-atomic electron Coulomb repulsive (J_1) and intra-orbital exchange potential (J_2).³¹ Here we employ the GGA+*U* (and LDA+*U*) scheme due to Dudarev³² for a better treatment of Co's 3d electrons; the meaningful term in this approach is $U_{\text{eff}} \equiv J_1 - J_2$, to which we refer hereafter simply as to U . The choice of the U value, however, is not unique or rigorously well defined. In general, this is selected so as to reproduce a particular set of experimental data (*e.g.*, lattice parameters or energy band gaps) or theoretical results obtained with higher accuracy methods as closely as possible.^{33–35}

Hybrid functionals represent a good alternative to DFT+*U* approximations. In this context, one mixes a particular amount of nonlocal Hartree–Fock (HF) exchange, α , with standard density functional (either LDA or GGA) exchange potentials. The resulting hybrid DFT exchange–correlation potential can be expressed as:

$$V_{\text{xc}}^{\text{hybrid}} = \alpha V_{\text{x}}^{\text{HF}} + (1 - \alpha) V_{\text{x}}^{\text{GGA/LDA}} + V_{\text{c}}^{\text{GGA/LDA}}, \quad (1)$$

where V_{x} and V_{c} represent exchange and correlation functionals, respectively. In contrast to GGA+*U* and LDA+*U*, hybrid functionals account for both the electronic localisation acting on all the states of the system and nonlocal exchange effects. Yet, in a strict *ab initio* sense, there is not a general prescription for choosing the right amount of nonlocal HF exchange.

In this work, we have used both the GGA+*U* (LDA+*U*) and hybrid functional approaches. Next, we explain the technical details of our calculations.

A. GGA+*U* calculations

In most of our calculations we used the generalised gradient approximation to density functional theory (DFT) proposed by Perdew, Burke, and Ernzerhof (PBE),³⁶ as it is implemented in the VASP package.³⁷ Other common exchange–correlation functional approximations such as LDA³⁸ and PBE^{sol}³⁹ were also considered. We used the “projector augmented wave” method to represent the ionic cores,⁴⁰ considering the following electrons as valence states: Co's 3p, 3d, and 4s; Sr's 4s, 5s, and 4p; and O's 2s and 2p. The wave functions were expanded in a plane-wave basis truncated at 500 eV, and a $\sqrt{2} \times \sqrt{2} \times 2$ simulation cell containing up to 20 atoms was used in most of our energy and geometry relaxation calculations (see Fig. 1a). For integrations in the Brillouin zone (BZ), we employed Γ -centered q -point grids of $8 \times 8 \times 8$. Using these parameters we obtained enthalpy energies that were converged to within 0.5 meV per formula unit (f.u.). Geometry relaxations were performed using a conjugate-gradient algorithm that varied the shape and in some cases also the volume of the unit cell; the imposed tolerance on the atomic forces was 0.01 eV \AA^{-1} . High-pressure equations of state were determined by computing the total energy of the crystal in a series of volume points that were subsequently fitted to analytical Birch–Murnaghan functions.⁴¹

We also calculated the vibrational phonon spectrum of several bulk phases by using the “direct method”^{42,43} and DFT calculations. In the direct method, the force-constant matrix of the crystal is calculated in real-space by considering the proportionality between atomic displacements and forces when the former are sufficiently small. Large supercells need to be constructed in order to guarantee that the elements of the force-constant matrix have all fallen off to negligible values at their boundaries, a condition that follows from the use of periodic boundary conditions.⁴⁴ Once the force-constant matrix is calculated one can Fourier-transform it to obtain the phonon spectrum at any q -point. The quantities with respect to which our phonon calculations need to be converged are the size of the supercell, the size of the atomic displacements, and the numerical accuracy in the sampling of the Brillouin zone. We found the following settings to provide zero-point energies¹⁰ converged to within 5 meV per f.u.: $2 \times 2 \times 2$ supercells containing up to 160 atoms, atomic displacements of 0.02 \AA , and q -point grids of $12 \times 12 \times 12$. The values of the phonon frequencies were obtained with the PHON code developed by Alfè.⁴⁴ In using this code we exploited the translational invariance of the system to impose the three acoustic branches to be exactly zero at the Γ q -point,

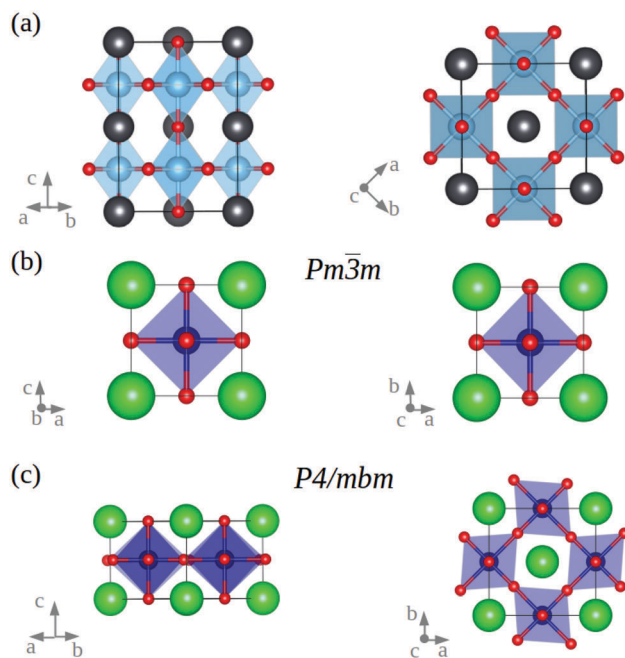


Fig. 1 (a) Sketch of the 20-atom $\sqrt{2} \times \sqrt{2} \times 2$ simulation cell used in most of our calculations; black, blue, and red spheres represent A, B, and O atoms in ABO₃ perovskites. The corresponding lattice vectors are $a_1 = (a, a, 0)$, $a_2 = (a, -a, 0)$, and $a_3 = (0, 0, 2a)$, where a is the lattice parameter of the 5-atom primitive perovskite cell. (b) Sketch of the cubic *Pm* $\bar{3}$ *m* phase. (c) Sketch of the tetragonal *P4/mbm* phase. Sr, Co, and O atoms are represented with green, blue, and red spheres, respectively.

and used central differences in the atomic forces (*i.e.*, positive and negative atomic displacements were considered).

B. Hybrid functional calculations

Hybrid functional DFT calculations were performed with the replicated-data version of the CRYSTAL14 package.⁴⁵ This is a first-principles electronic structure software program which employs atom-centered Gaussian-type orbital (GTO) basis sets to build Bloch functions that represent the one-electron crystalline orbitals. GTO offers a number of convenient computational features, *e.g.*, the use of local basis sets containing minimal overlap with neighboring orbitals, which allow us to perform HF exchange calculations in medium and large size systems affordably (*e.g.*, the resulting computational expense scales as N^{2-3} with the number of particles, to be compared with the usual N^4 scaling found in plane-wave based methods). All-electron GTO atomic basis sets were chosen as follows: for Co atoms we used the double-zeta all-electron basis set from ref. 46 for Sr atoms small-core Hay-Wadt pseudopotentials⁴⁷ were adopted for the description of the inner-shell electrons 1s, 2s, 2p, 3s, 3p, and 3d, while for the valence parts 4s, 4p, and 5s we used the optimized basis set successfully applied to the strontium titanate study,⁴⁸ and for O atoms we used the 8–411d all-electron basis set constructed by Corà.⁴⁹

A Monkhorst-Pack $8 \times 8 \times 8$ *q*-point grid was used for BZ sampling. The thresholds controlling the accuracy in the calculation of the Coulomb and exchange integrals were set

equal to 10^{-7} and 10^{-14} , and to 10^{-7} eV in the SCF energy. The crystal cell parameters and atomic positions were relaxed during the geometry optimisations by imposing a convergence criterion of $0.008 \text{ eV \AA}^{-1}$ in the atomic forces. The hybrid functionals employed in this study include PBE-10,³⁵ PBE0,⁵⁰ and HSE06.⁵¹ In the first two versions, the amount of HF exchange is 0.10 and 0.25, respectively (that is, parameter α in eqn (1)); in the HSE06 case, there is an additional separation between short and long ranges in which parameters $\alpha = 0.25$ and 1.00 are used, respectively.

III. Results and discussion

A. Intermediate spin state and the choice of *U*

There is strong experimental and theoretical evidence showing that bulk SCO possesses an intermediate spin (IS) state resulting from a competition between intra-atomic exchange interactions and the crystal field.^{18–21} (The experimental evidence consists of SQUID measurements of saturated Co magnetic moments;¹⁸ the theoretical evidence consists of previous atomic-multiplet, Hartree–Fock, and DFT-based studies.^{19–21}) This IS configuration can be understood as a high spin state in the Co³⁺ ions that is antiferromagnetically coupled to a ligand hole of *e_g* symmetry, which can be formally represented with the d-orbital occupation model $t_{2g}^4 e_g^1$ (see Fig. 2a).^{19,21} In Fig. 2b, we show the partial density of electronic d states (pDOS) calculated in bulk SCO in the cubic *Pm* $\bar{3}$ *m* phase with the hybrid functional HSE06⁵¹ (see Fig. 1b); our hybrid functional pDOS results reproduce the expected orbital occupation configuration $t_{2g}^4 e_g^1$: two unoccupied t_{2g}^{\downarrow} states (d_{xz} and d_{yz} above the Fermi energy level, E_F) and one occupied t_{2g}^{\downarrow} state (d_{xy} below E_F), while *e_g* states are smeared over a large energy range containing E_F in the spin-up channel. Analogous d-orbital pDOS results (not shown here) were obtained with the hybrid functional PBE0.⁵⁰

In Fig. 3, we show the d-orbital pDOS calculated also in bulk SCO considering the cubic *Pm* $\bar{3}$ *m* phase but employing the GGA+*U* method. Several *U* values were employed in order to analyse the effect of this term on the description of the expected IS state. It is found that only for $U > 5$ eV the IS state in bulk SCO is reproduced correctly, as otherwise a low spin state is obtained (that is, no particular d state is unoccupied). For instance, in the $U = 6$ eV case the two unoccupied t_{2g}^{\downarrow} states (d_{xz} and d_{yz} above E_F) are correctly reproduced whereas in the $U = 2$ and 4 eV cases those appear as partially occupied. We note that these conclusions are in agreement with the recent results reported by Hoffmann *et al.* in ref. 21. In view of these findings, we adopted $U = 6$ eV for the rest of our GGA+*U* (and LDA+*U*) calculations. It is worth noticing that in previous GGA+*U* studies by Lee and Rabe^{29,30} values of $U < 5$ eV were employed instead, hence the d-orbital configurations sampled therein are likely to differ from the expected IS state.

B. Bulk SrCoO₃ at equilibrium

In all our GGA+*U*, LDA+*U* and hybrid functional DFT calculations, we consistently found that a tetragonal *P4/mbm* phase displaying

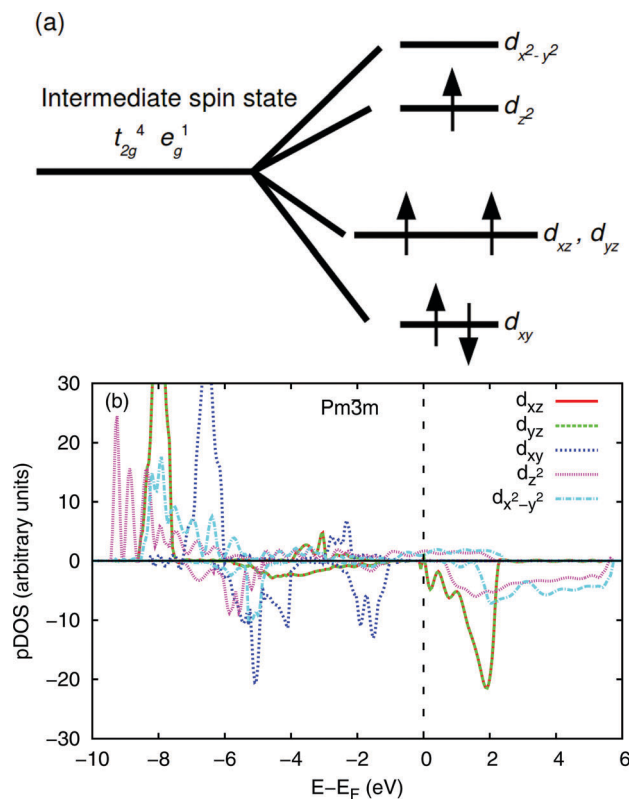


Fig. 2 (a) Sketch of a possible intermediate spin state expected to occur in bulk SrCoO_3 .¹⁹ (b) Density of electronic d states calculated for bulk SrCoO_3 in a cubic $Pm\bar{3}m$ phase with the HSE06 hybrid functional. Spin-up and spin-down electronic densities are represented with positive and negative values, respectively.

moderate Jahn–Teller distortions and a c/a ratio of $\sim 1/\sqrt{2}$ (see Fig. 1c) has a lower energy than the cubic $Pm\bar{3}m$ phase, thus far assumed to be the ground-state in bulk SCO.^{16–18} In particular, the new tetragonal $P4/mbm$ phase (space group 127) has a 10-atom unit cell in which two Co atoms sit on c Wyckoff positions, two Sr atoms on a Wyckoff positions, two apical O atoms on d Wyckoff positions, and four equatorial O atoms on h Wyckoff positions. The Jahn–Teller (JT) distortions that are relevant to this structure can be expressed as:

$$Q_2 = \frac{2(l-s)}{\sqrt{2}}, \quad (2)$$

$$Q_3 = \frac{2(2m-l-s)}{\sqrt{6}}, \quad (3)$$

where l , m , and s refer to the long, medium and short Co–O distances, respectively (see Fig. 4). A third possible JT distortion associated with a breathing mode, Q_1 (see Fig. 4), was found to be negligible in bulk SCO.

In Table 1, we summarise our energy, structural, and magnetic results obtained in the new tetragonal $P4/mbm$ phase. As it is appreciated therein, the energy difference between the tetragonal $P4/mbm$ and cubic $Pm\bar{3}m$ phases, $\Delta E \equiv E(P4/mbm) - E(Pm\bar{3}m)$, is of the order of ~ 0.1 eV per f.u., that is, fairly large, with hybrid

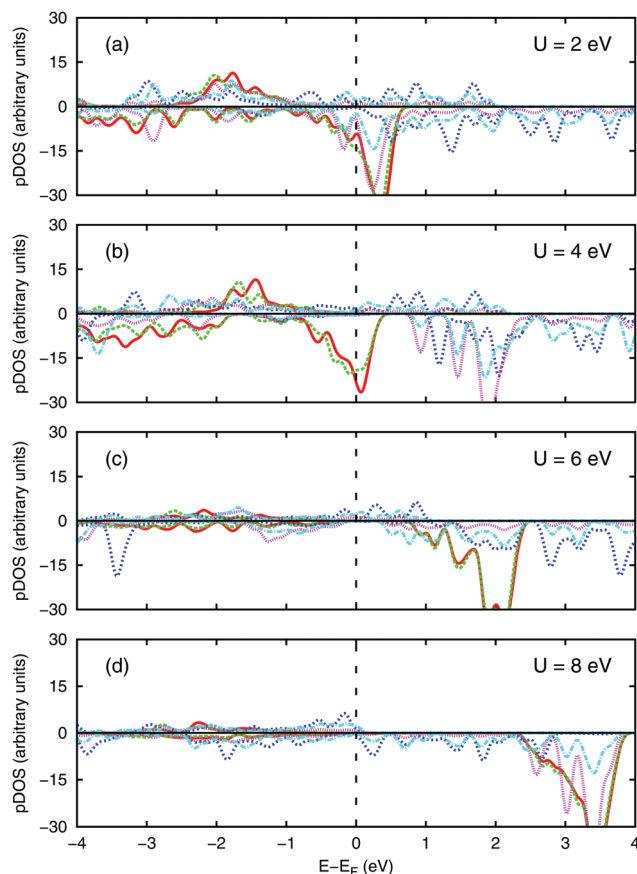


Fig. 3 Density of electronic d states calculated in bulk SrCoO_3 in the cubic $Pm\bar{3}m$ phase with the PBE+ U method expressed as a function of U . Spin-up and spin-down electronic densities are represented with positive and negative values, respectively. The convention in representing the d states is the same as in the previous figure. U values smaller than 5 eV do not reproduce the expected intermediate spin state in bulk SCO.

functionals providing the largest $|\Delta E|$ values. In most cases the predicted magnetic moment per Co ion is of $2.5\text{--}2.9 \mu_B$, which is consistent with the expected intermediate spin state.^{18–21} Regarding the structural features, all DFT functionals render a c/a ratio of $\sim 1/\sqrt{2}$, which denotes very small tetragonality as the unit cell of the $P4/mbm$ phase can be thought of a $\sqrt{2} \times \sqrt{2} \times 1$ supercell constructed from the usual 5-atom perovskite unit cell. The x displacement associated with h Wyckoff positions, which are occupied by equatorial oxygen atoms, varies from 0.23 to 0.27 depending on the employed functional. Finally, the Q_2 JT distortion, which mostly affects the equatorial plane in the oxygen octahedra (see Fig. 4), appears to be dominant.

It is worth mentioning that the value of the U parameter has a noticeable effect on the final energy, magnetic, and structural results which are obtained with GGA+ U methods (besides its role in the description of the intermediate spin state that is observed in bulk SCO, see Section III A). For instance, in Table 1 we show that the energy difference ΔE increases from -126 to -51 meV per f.u. as the value of U decreases from 6.0 to 1.5 eV (*i.e.*, compare cases PBE+ U and PBE+ U^* therein). The rest of the magnetic and structural parameters enclosed in Table 1 also

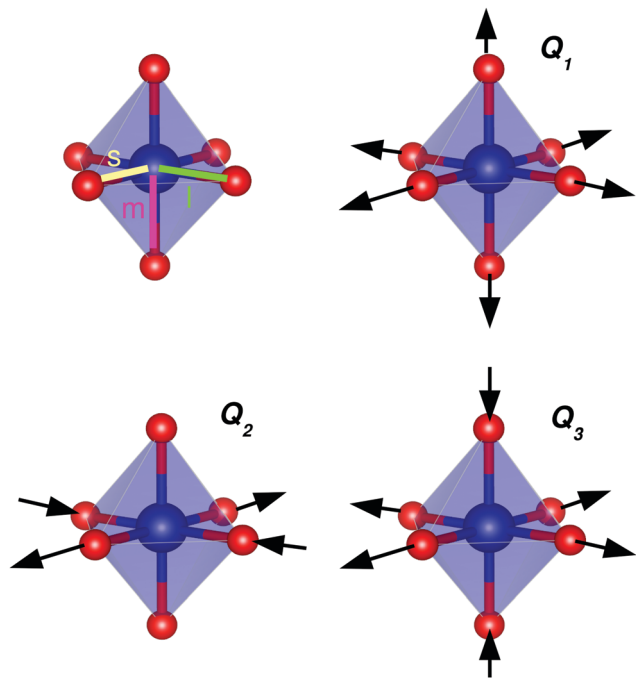


Fig. 4 Sketch of the possible Jahn–Teller distortion modes in SrCoO₃ and of the distorted Co–O bonds *l*, *m*, and *s*.

Table 1 Energy, structural, and magnetic properties of bulk equilibrium SrCoO₃ calculated in the tetragonal *P4/mbm* phase using several hybrid and DFT functionals ($U = 6.0$ and $U^* = 1.5$ eV). $\Delta E \equiv E(P4/mbm) - E(Pm\bar{3}m)$, M is the magnetic moment per Co ion, a , b , c , the length of the lattice vectors, x the displacement of the equatorial O atoms sitting in h Wyckoff positions, and Q_2 and Q_3 lattice Jahn–Teller distortion parameters (see the text)

	ΔE (meV per f.u.)	M (μ_B)	a (Å)	b (Å)	c (Å)	x	Q_2 (Å)	Q_3 (Å)
HSE06	−310	2.53	5.429	5.429	3.912	0.272	0.474	0.060
PBE0	−269	2.50	5.424	5.424	3.909	0.227	0.498	0.060
PBE+10	−158	2.28	5.392	5.392	3.979	0.233	0.376	0.136
PBE+ U	−126	2.84	5.502	5.502	3.943	0.268	0.397	0.042
PBE ^{sol} + U	−117	2.78	5.404	5.404	3.873	0.266	0.345	0.042
LDA+ U	−109	2.86	5.313	5.313	3.811	0.265	0.324	0.044
PBE+ U^*	−51	2.28	5.400	5.400	4.000	0.264	0.307	0.148

change considerably when U is varied. Nevertheless, we consistently find that the tetragonal *P4/mbm* phase is predicted to have the lowest zero-temperature energy in all the cases.

We have calculated the d-orbital pDOS of bulk SCO in the new tetragonal *P4/mbm* phase with the hybrid functional HSE06 (see Fig. 5b). Our results reproduce the expected orbital occupation configuration $t_{2g}^4 e_g^1$: two unoccupied t_{2g}^{\downarrow} states (d_{xy} and d_{yz}/d_{xz} above E_F) and one occupied t_{2g}^{\downarrow} state (d_{yz}/d_{xz} below E_F), while e_g states are smeared over a large energy range containing E_F in the spin-up channel. The main effect deriving from the presence of JT distortions and lowering of crystal symmetry as compared to the cubic *Pm\bar{3}m* phase is to swap the energy ordering between t_{2g} d-states (see Fig. 2a and 5a). Analogous d-orbital pDOS results were obtained with the PBE+ U and hybrid PBE0 and PBE-10 functionals.

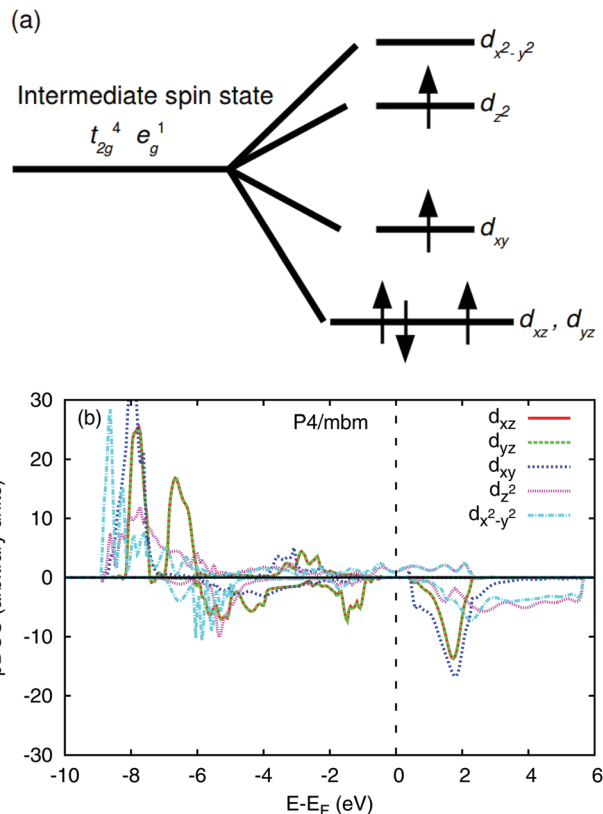


Fig. 5 (a) Sketch of a possible intermediate spin state expected to occur in bulk SrCoO₃.¹⁹ (b) Density of electronic d states calculated for bulk SrCoO₃ in a tetragonal *P4/mbm* phase with the HSE06 hybrid functional. Spin-up and spin-down electronic densities are represented with positive and negative values, respectively.

We calculated the lattice phonon spectrum of bulk SCO in the new tetragonal *P4/mbm* phase with the PBE+ U method. It was found that this structure is vibrationally and mechanically stable as no imaginary phonon frequency appeared in the corresponding Brillouin zone (see Fig. 6). Interestingly, we performed analogous phonon calculations in the cubic *Pm\bar{3}m* phase and found few imaginary phonon frequencies at the high-symmetry reciprocal-space point $M = \left(\frac{1}{2} \frac{1}{2} 0\right)$. This finding

is consistent with the fact that by enlarging the 5-atom perovskite unit cell along the x - y Cartesian directions it is possible to find a lower-energy crystal structure at zero temperature. Also, it suggests that SCO in the cubic *Pm\bar{3}m* phase may be highly anharmonic. With regard to the latter point, it could be possible then that the cubic *Pm\bar{3}m* phase was entropically stabilised over the tetragonal *P4/mbm* phase at $T \neq 0$ K conditions;^{52,53} this possibility, however, has not been explored in the present work.

C. Bulk SrCoO₃ under pressure

Under compression, oxide perovskites may undergo phase transformation into higher symmetry configurations.^{54,55} For this reason, we analysed the possibility of a P -induced *P4/mbm* \rightarrow *Pm\bar{3}m* phase transition in bulk SCO with the PBE+ U method. In Fig. 7a, we show the zero-temperature enthalpy difference

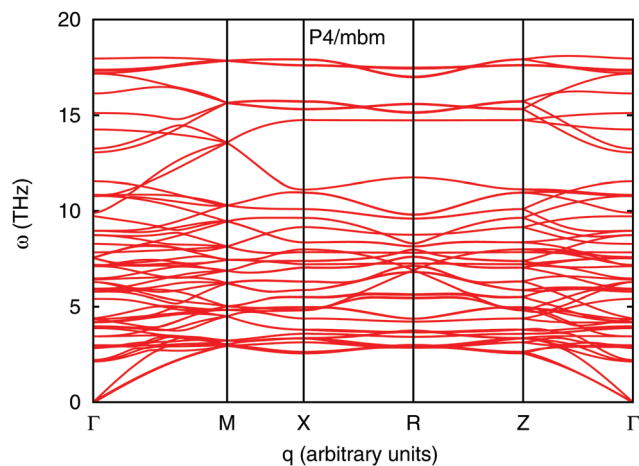


Fig. 6 Lattice phonon spectrum calculated for bulk SrCoO_3 in a tetragonal $P4/mbm$ phase with the PBE+ U method ($U = 6$ eV).

calculated between the two phases, $\Delta H \equiv H(P4/mbm) - H(Pm\bar{3}m)$, expressed as a function of pressure. As it is observed therein, the effect of compression initially is to reduce the value of $|\Delta H|$, however, at $P > 45$ GPa this trend is reverted. Such a change of tendency is due to the disappearance of an energy band gap in the spin-down channel of the cubic $Pm\bar{3}m$ phase (not shown here); the d-orbital pDOS estimated in the tetragonal $P4/mbm$ phase, in contrast, always displays an intermediate spin state in the interval $0 \leq P \leq 70$ GPa.

Analogous zero-temperature enthalpy calculations were performed also with the hybrid functional HSE06. The results obtained in this case are fully consistent with the conclusions found with the PBE+ U method, that is, the tetragonal $P4/mbm$ phase remains in the ground state in the pressure interval $0 \leq P \leq 70$ GPa and under further compression. We note that the ΔH values obtained with the PBE+ U and HSE06 methods are in reasonably good agreement. For instance, at the pressure points 10 and 70 GPa the hybrid functional provides enthalpy energy differences of -0.025 and -0.022 eV per f.u., respectively, to be compared with values -0.047 and -0.030 eV per f.u. obtained with PBE+ U .

In a recent experimental study on bulk SCO at $T = 200$ K, Yang *et al.* have reported two P -induced phase transitions occurring at $P \sim 1$ and ~ 45 GPa which involve a spin reorientation and spin-state change, respectively.⁵⁶ These observations are not coincident with our results obtained in bulk stoichiometric SCO. The reasons behind such a disagreement could be explained in terms of (i) the neglect of thermal excitations in our theoretical study, and/or (ii) the presence of small oxygen deficiencies in the experimental samples (*i.e.*, $\text{SrCoO}_{3-\delta}$ with $\delta = 0.05$, as reported by Yang *et al.*⁵⁶). In order to substantiate the effects of small non-stoichiometry in bulk SCO under pressure (at zero temperature), we calculated the enthalpy of $\text{SrCoO}_{2.75}$ crystals (that is, generated by removing one oxygen atom from the stoichiometric 20-atom unit cell) as a function of pressure. We considered four possible magnetic spin arrangements: ferromagnetic (FM), antiferromagnetic A-type (A-A, parallel in-plane spins, antiparallel out-of-plane spins), antiferromagnetic G-type (A-G, antiparallel in-plane spins,

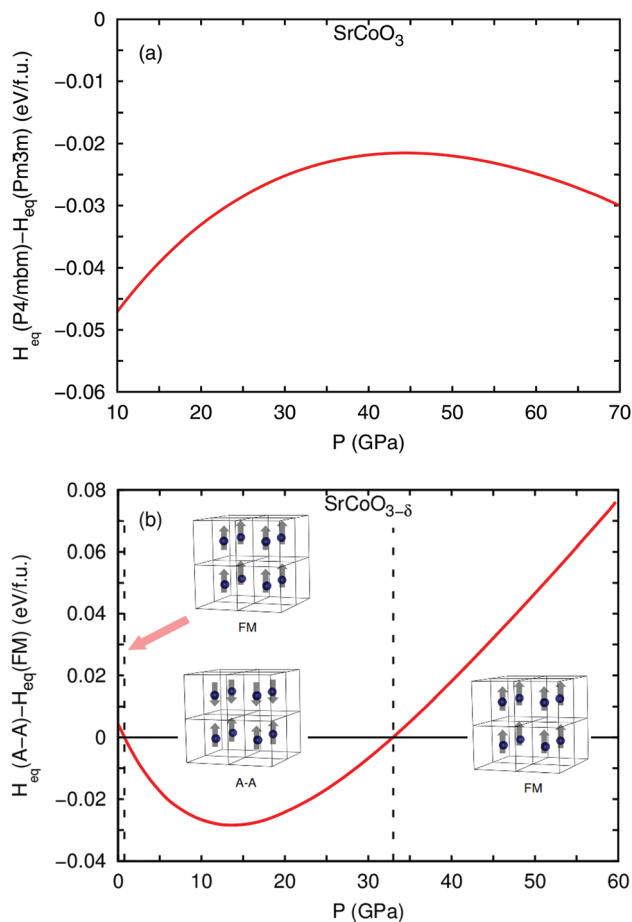


Fig. 7 (a) Enthalpy energy difference between the tetragonal $P4/mbm$ and cubic $Pm\bar{3}m$ phases calculated in stoichiometric SCO as a function of pressure. (b) Enthalpy energy difference between magnetic spin orders A-A and FM calculated in non-stoichiometric SCO ($\text{SrCoO}_{2.75}$) as a function of pressure. The vertical dashed lines indicate P -induced phase transitions affecting the magnetic spin order.

antiparallel out-of-plane spins), and antiferromagnetic C-type (A-C, antiparallel in-plane spins, parallel out-of-plane spins).

In Fig. 7b, we plot the zero-temperature enthalpy difference calculated among the lowest-energy $\text{SrCoO}_{2.75}$ configurations obtained when constraining ferromagnetic (FM) and antiferromagnetic A-type (A-A) spin orders, $\Delta H^m \equiv H^{A-A} - H^{FM}$, as those were found to be the energetically most favorable cases. It is observed that at $P \sim 0$ GPa the enthalpy difference ΔH^m adopts very small and positive values, which indicates that FM spin order remains the most stable; however, when pressure is increased beyond 0.75 GPa the system with A-A spin order becomes the ground state. We note that this transition point is very close to the pressure at which Yang *et al.* have observed a reorientation of magnetic spins in SCO (*i.e.*, 1.1 GPa⁵⁶); nevertheless, our calculated ΔH^m values within the pressure interval $0 \leq P \leq 1$ GPa are so small (*i.e.*, of the order of our accuracy threshold of ~ 1 meV per f.u.) that we cannot discard that bulk $\text{SrCoO}_{2.75}$ is already antiferromagnetic close to the equilibrium point. As pressure is increased beyond 33 GPa, FM spin order clearly provides the lowest energy. According to our calculations,

such a magnetic A → FM phase transformation is accompanied by a very small volume reduction of 0.8%, in which the volume of the A-A phase is 49.15 Å³.

In view of our zero-temperature results obtained in bulk SrCoO_{3-δ} under pressure, Yang *et al.*'s observations reported at $P \sim 45$ GPa⁵⁶ could be reinterpreted as a full magnetic spin order transformation, rather than as a spin-state change. In fact, the phase transition that we report in SrCoO_{2.75} is isostructural and continuous, as it has been observed in the laboratory. However, no intermediate to low spin state transition is observed in our calculations, neither in the stoichiometric nor in the nonstoichiometric case, when considering the lowest-energy phases. Further experimental studies in compressed SCO are highly desirable in order to rigorously confirm or reject our hypothesis.

D. SrCoO₃ thin films

Lee and Rabe have recently predicted a series of intriguing multiferroic phase transformation occurring in stoichiometric SCO thin films, based on GGA+*U* DFT calculations.^{29,30} In particular, it has been proposed that both small tensile and compressive epitaxial strains (*i.e.*, of $\sim +3\%$ and $\sim -1\%$, respectively) can trigger a transformation from the bulk FM-metallic phase into an A-insulating-ferroelectric phase. These theoretical results suggest that large magnetoelectric effects, that is, cross responses to applied electric and magnetic fields, could be realised in SCO

thin films, as in regions where several multiferroic phases are energetically competitive those can be expected to occur.^{57,58} In two recent experimental studies on SrCoO_{3-δ} thin films by Callori *et al.*²⁶ and Hu *et al.*,²⁷ the existence of an antiferromagnetic phase at moderate tensile strains of $\sim +2.7\%$ has been ascertained; however, the accompanying metal-to-insulator and nonpolar-to-ferroelectric phase transitions as predicted by Lee and Rabe appear to be missing. The second multiferroic phase transformation that has been anticipated to occur at compressive strains also remains experimentally unverified, in spite of the small epitaxial distortions that have been suggested to be involved (*i.e.*, $\sim -1\%$).^{29,30}

In view of the results presented in previous sections, we considered as opportune to revise the zero-temperature phase diagram of stoichiometric SCO thin films that is obtained with first-principles methods. We employed the PBE+*U* method with $U = 6$ eV, in order to reproduce the expected intermediate spin state correctly (see Section III A). In addition to the tetragonal $P4/mbm$ and cubic $Pm\bar{3}m$ phases considered so far in this study (we note that the latter phase transforms into tetragonal $P4/mmm$ when exerting epitaxial constraints on it), we analysed many other structures exhibiting tetragonal (*e.g.*, $P4mm$, $P4cc$, and $P4_2/mnm$), orthorhombic (*e.g.*, $Amm2$, $Pna2_1$, and $Pmc2_1$) and monoclinic (*e.g.*, $C2/m$, $P2/m$, and $P2_1/c$) crystalline symmetry. All those structures were considered in the four magnetic spin arrangements that can be reproduced with our 20-atom simulation cell, namely, FM, A-A, A-C, and A-G (see Section III C).

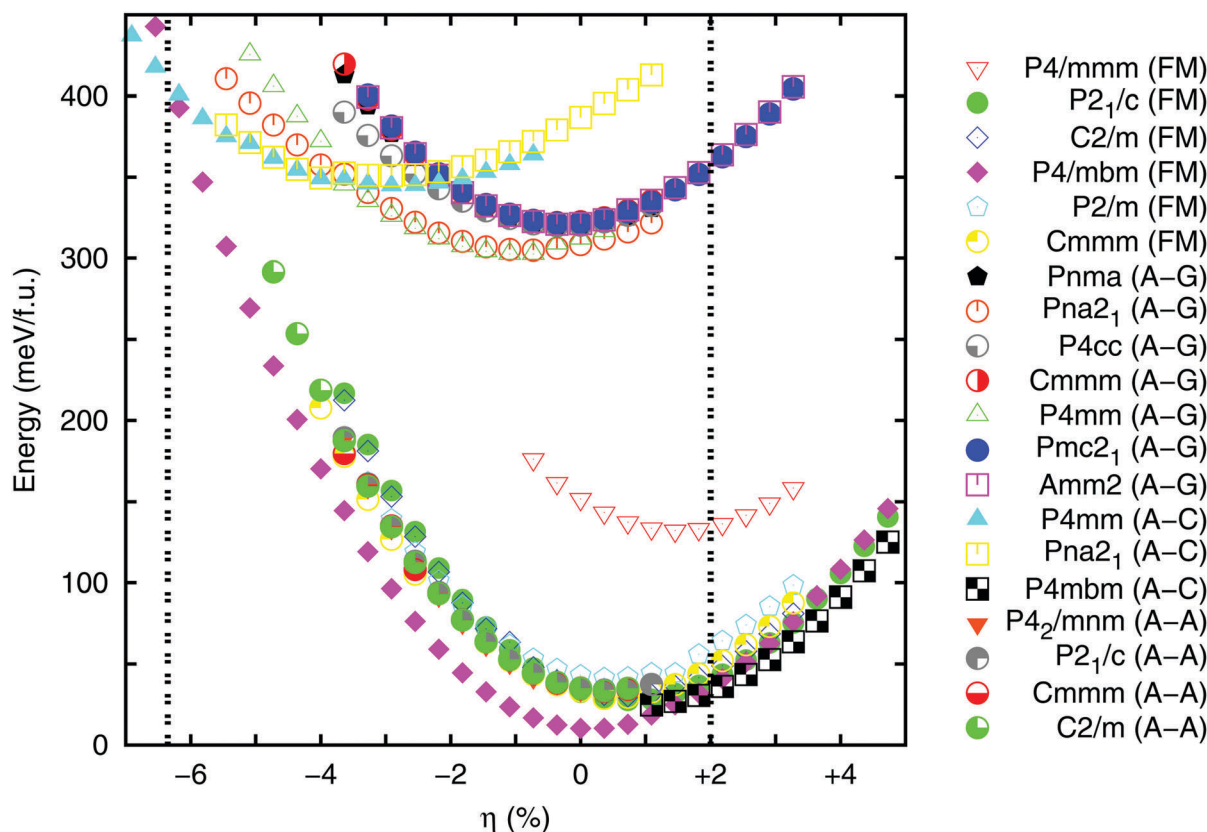


Fig. 8 Energy of several competitive phases in SrCoO₃ thin films calculated as a function of epitaxial strain. The vertical dashed lines indicate η -induced phase transitions affecting the structural, magnetic, and electronic properties of the system.

In Fig. 8, we represent the zero-temperature energy of the crystal phases that according to our DFT calculations are energetically most competitive in stoichiometric SCO thin films (some irrelevant magnetic order phases have been omitted for clarity) as a function of epitaxial strain, $\eta [= (a - a_0)/a_0]$, where a_0 is equal to 3.89 Å. Interestingly, we found an extreme and complex competition between FM and A-A phases, including tetragonal, orthorhombic and monoclinic crystals, at $\eta \sim 0\%$ conditions. In particular, the energy of the orthorhombic $Cmmm$ and monoclinic $C2/m$ and $P2_1/c$ phases, either in the FM or A-A magnetic spin arrangements, is just ~ 20 meV per f.u. above that of the tetragonal $P4/mbm$ phase (FM case). (We note that none of these low-energy structures was considered by Lee and Rabe in works.^{29,30}) Such a fierce phase competition appears to be comparable to that found in archetypal multiferroic compounds like, for instance, BiFeO_3 .⁵⁹ Meanwhile, under small epitaxial strain conditions phases displaying A-C and A-G magnetic spin orders are found to be energetically noncompetitive, the tetragonal $P4/mbm$ phase (A-C case) being the exception.

At $\eta = +2.0\%$, we found that the tetragonal ground-state phase undergoes a magnetic phase transition from FM to A-C (see vertical dashed lines in Fig. 8). (The same strain-induced

phase transition is predicted to occur at $\eta = +2.4\%$ with the hybrid functional HSE06.) This is a continuous and isostructural phase transformation. In order to identify possible electronic-structure changes associated with this transition, we calculated the d-orbital pDOS in the two relevant $P4/mbm$ phases (see Fig. 9). Our results suggest a change from an intermediate spin state in the FM phase to a low spin state in the A-C phase, as in the latter case no energy band gap appears in the spin-down channel. Likewise, along the tensile strain-induced phase transition the system is likely to improve its electrical conductivity properties rather than becoming an insulator (in contrast to the $P4/mmm \rightarrow Pmc2_1$ transformation suggested in ref. 29 and 30, which renders an insulator and ferroelectric compound at $\eta \sim +3\%$). Our predictions appear to be consistent with recent experimental observations reported by Callori *et al.*²⁶ and Hu *et al.*²⁷ Nevertheless, new detailed experiments characterising the structural and electronic features of SCO thin films at moderate tensile strains appear to be necessary for resolving the discrepancies found between ours and previous DFT studies.^{29,30}

At $\eta = -6.4\%$, we found that the system transforms into a tetragonal $P4mm$ phase displaying A-C spin order and a large c/a ratio of ~ 1.3 (see vertical dashed lines in Fig. 8). (The same

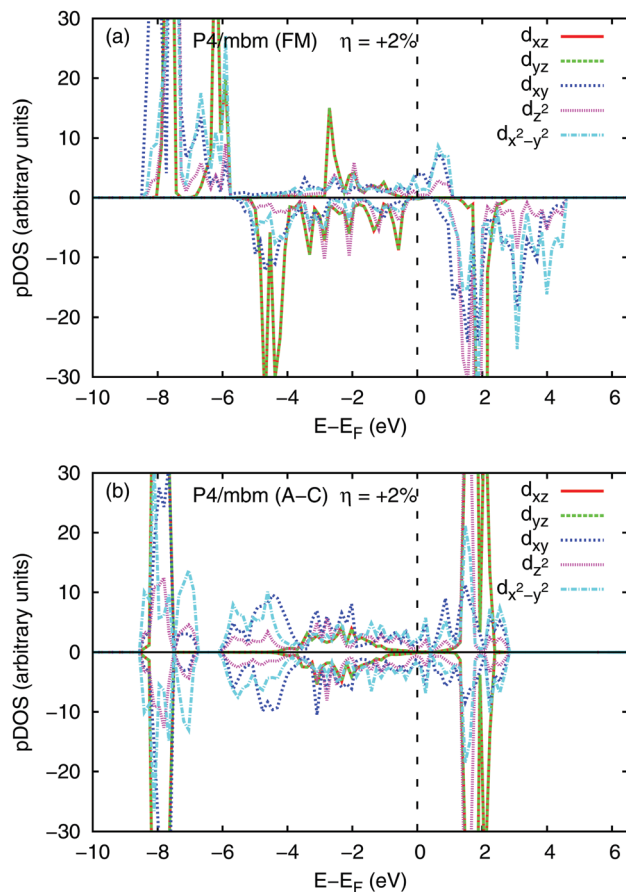


Fig. 9 Density of electronic d states calculated with the PBE+ U method ($U = 6$ eV) in tensile SrCoO_3 thin films in the tetragonal (a) $P4/mbm$ [FM] and (b) $P4/mbm$ [A-C] phases. Spin-up and spin-down electronic densities are represented with positive and negative values, respectively.

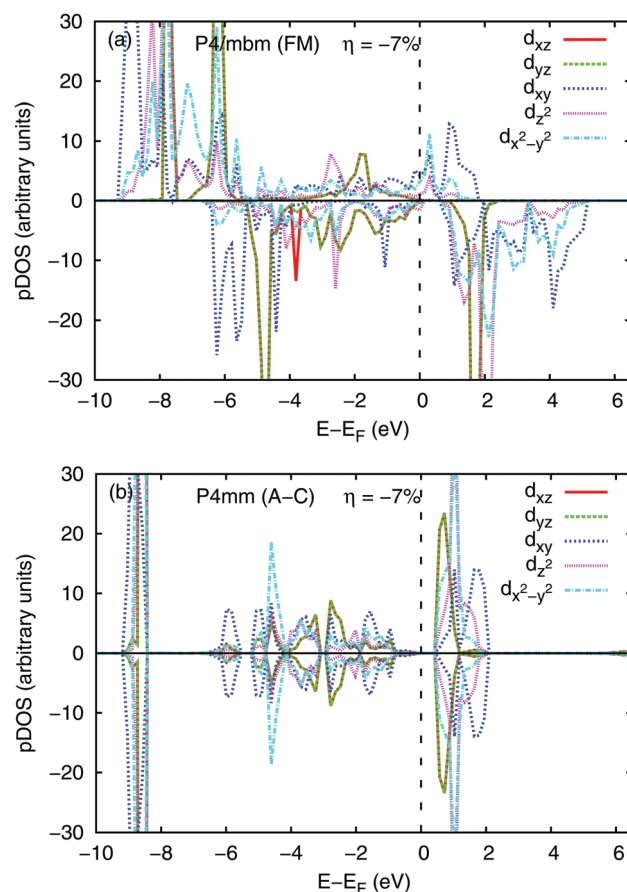


Fig. 10 Density of electronic d states calculated with the PBE+ U method ($U = 6$ eV) in highly compressive SrCoO_3 thin films in the tetragonal (a) $P4/mbm$ [FM] and (b) $P4mm$ [A-C] phases. Spin-up and spin-down electronic densities are represented with positive and negative values, respectively.

strain-induced phase transition is predicted to occur at $\eta = -5.5\%$ with the hybrid functional HSE06.) In order to identify the possible electronic-structure changes associated with this transition, we calculated the d-orbital pDOS in the two involved tetragonal phases (see Fig. 10). Our analysis reveals that SCO $P4mm$ (A–C) thin films are insulator and also ferroelectric, in particular they exhibit a large out-of-plane electrical polarisation of $\sim 115 \text{ mC m}^{-2}$ (as it has been estimated with the methods introduced in work⁶⁰). The predicted phase transition, therefore, involves a three-fold structural, magnetic, and ferroelectric transformation; however, in spite of its fundamental and technological interests, it requires of so large compressive strains that it would be hardly realisable in practice (in contrast to the multiferroic phase transformation predicted by Lee and Rabe at $\eta \sim -1\%$ ^{29,30}). Nonetheless, we found that the same type of phase transformation occurs in nonstoichiometric SCO thin films (*i.e.*, $\text{SrCoO}_{2.75}$) at a smaller critical epitaxial strain of $\eta = -5.4\%$. Magnetoelectric effects, therefore, are probably more likely to be observed in nonstoichiometric SCO samples than in stoichiometric.

IV. Summary

We have presented a thorough revision of the zero-temperature phase diagram of stoichiometric SrCoO_3 that is obtained with first-principles methods based on density functional theory (*i.e.*, GGA+ U and hybrid functionals). In the bulk case, we have identified a tetragonal $P4/mbm$ phase with moderate JT distortions and a c/a ratio of $\sim 1/\sqrt{2}$ as the ground state of the system. The same phase remains the most stable as hydrostatic pressures of up to $\sim 70 \text{ GPa}$ are applied. This central result either calls for a revision of previous crystallographic data gathered in SCO at low temperatures, or it well represents a failure of DFT methods in describing such a highly correlated oxide compound. In SCO thin films, we have found two phase transitions occurring at moderate tensile and large compressive epitaxial strains (*i.e.*, $\sim +2\%$ and $\sim -6\%$, respectively). According to our calculations, the first transformation is isostructural and comprises only a change in magnetic spin order. The second transition, in contrast, involves a three-fold structural, magnetic, and polar transformation; however, the critical epitaxial strain associated with this transition is so large that it appears to be irrealisable in practice. The general description of SCO thin films that follows from our study appears to be consistent with recent experimental observations, however, it differs considerably from the previously reported DFT GGA+ U results. The main reason behind such a disagreement is likely to be related to the choice of the U value, which as we have shown has an important effect on the description of the electronic and magnetic spin degrees of freedom. New and systematic experiments on stoichiometric SCO, both in bulk and thin film geometries, certainly are necessary in order to advance our knowledge of this intriguing material.

Acknowledgements

This research was supported by the Australian Research Council under Future Fellowship funding scheme (Grant No. FT140100135).

Computational resources and technical assistance were provided by the Australian Government through Magnus under the National Computational Merit Allocation Scheme. P. R. acknowledges an allocation of computing time from the Louisiana State University High Performance Computing center.

References

- 1 A. J. Hatt and N. A. Spaldin, *Phys. Rev. B: Condens. Matter Mater. Phys.*, 2010, **82**, 195402.
- 2 J. M. Rondinelli and N. A. Spaldin, *Adv. Mater.*, 2011, **23**, 3363.
- 3 J. M. Rondinelli and S. Coh, *Phys. Rev. Lett.*, 2011, **106**, 235502.
- 4 S. J. May, J.-W. Kim, J. M. Rondinelli, E. Karapetrova, N. A. Spaldin, A. Bhattacharya and P. J. Ryan, *Phys. Rev. B: Condens. Matter Mater. Phys.*, 2010, **82**, 014110.
- 5 C. Cazorla and M. Stengel, *Phys. Rev. B: Condens. Matter Mater. Phys.*, 2014, **90**, 020101(R).
- 6 C. Cazorla and M. Stengel, *Phys. Rev. B: Condens. Matter Mater. Phys.*, 2015, **92**, 214108.
- 7 C. W. Swartz and X. Wu, *Phys. Rev. B: Condens. Matter Mater. Phys.*, 2012, **85**, 054102.
- 8 M. Stengel, C. J. Fennie and Ph. Ghosez, *Phys. Rev. B: Condens. Matter Mater. Phys.*, 2012, **86**, 094112.
- 9 J. Hong and D. Vanderbilt, *Phys. Rev. B: Condens. Matter Mater. Phys.*, 2013, **87**, 064104.
- 10 C. Cazorla and J. Íñiguez, *Phys. Rev. B: Condens. Matter Mater. Phys.*, 2013, **88**, 214430.
- 11 S. D. Ganichev, E. L. Ivchenko, S. N. Danilov, J. Eroms, W. Wegscheider, D. Weiss and W. Prettl, *Phys. Rev. Lett.*, 2001, **86**, 4358.
- 12 U. Lüders, A. Barthélémy, M. Bibes, K. Bouzehouane, S. Fusil, E. Jacquet, J.-P. Contour, J.-F. Bobo, J. Fontcuberta and A. Fert, *Adv. Mater.*, 2006, **18**, 1733.
- 13 M. Gajek, M. Bibes, S. Fusil, K. Bouzehouane, J. Fontcuberta, A. Barthélémy and A. Fert, *Nat. Mater.*, 2007, **6**, 296.
- 14 H. Jeon, W. S. Choi, M. D. Biegalski, C. M. Folkman, I.-C. Tung, D. D. Fong, J. W. Freeland, D. Shin, H. Ohta, M. F. Chisholm and H. N. Lee, *Nat. Mater.*, 2013, **12**, 1057.
- 15 H. Jeon, W. S. Choi, J. W. Freeland, H. Ohata, C. U. Jung and H. N. Lee, *Adv. Mater.*, 2013, **25**, 3651.
- 16 P. Bezdicka, A. Wattiaux, J. C. Grenier, M. Pouchard and P. Hagenmuller, *Z. Anorg. Allg. Chem.*, 1993, **619**, 7.
- 17 S. Kawasaki, M. Takano and Y. Takeda, *J. Solid State Chem.*, 1996, **121**, 174.
- 18 Y. Long, Y. Kaneko, S. Ishiwata, Y. Taguchi and Y. Tokura, *J. Phys.: Condens. Matter*, 2011, **23**, 245601.
- 19 R. H. Potze, G. A. Sawatzky and M. Abbate, *Phys. Rev. B: Condens. Matter Mater. Phys.*, 1995, **51**, 11501.
- 20 M. Zhuang, W. Zhang, A. Hu and N. Ming, *Phys. Rev. B: Condens. Matter Mater. Phys.*, 1998, **57**, 13655.
- 21 M. Hoffmann, V. S. Borisov, S. Ostanin, I. Mertig, W. Hergert and A. Ernst, *Phys. Rev. B: Condens. Matter Mater. Phys.*, 2015, **92**, 094427.
- 22 T. Takeda, H. Watanabe and Y. Yamaguchi, *J. Phys. Soc. Jpn.*, 1972, **33**, 970.

- 23 H. Taguchi, M. Shimada and M. Koizumi, *J. Solid State Chem.*, 1979, **29**, 221.
- 24 C. K. Xie, Y. F. Nie, B. O. Wells, J. I. Budnick, W. A. Hines and B. Dabrowski, *Appl. Phys. Lett.*, 2011, **99**, 052503.
- 25 W. S. Choi, H. Jeon, S. S. A. Seo, V. R. Cooper, K. M. Rabe and H. N. Lee, *Phys. Rev. Lett.*, 2013, **111**, 097401.
- 26 S. J. Callori, S. Hu, J. Bertinshaw, Z. J. Yue, S. Danilkin, X. L. Wang, N. Valanoor, F. Klose, J. Seidel and C. Ulrich, *Phys. Rev. B: Condens. Matter Mater. Phys.*, 2015, **91**, 140405(R).
- 27 S. Hu, Z. Yue, J. S. Lim, S. J. Callori, J. Bertinshaw, A. Ikeda-Ohno, T. Ohkochi, C.-H. Yang, X. Wang, C. Ulrich and J. Seidel, *Adv. Mater. Interfaces*, 2015, **2**, 1500012.
- 28 J. R. Petrie, C. Mitra, H. Jeon, W. S. Choi, T. L. Meyer, F. A. Reboredo, J. W. Freeland, G. Eres and H. N. Lee, *Adv. Funct. Mater.*, 2016, **26**, 1564.
- 29 J. H. Lee and K. M. Rabe, *Phys. Rev. Lett.*, 2011, **107**, 067601.
- 30 J. H. Lee and K. M. Rabe, *Phys. Rev. B: Condens. Matter Mater. Phys.*, 2011, **84**, 104440.
- 31 A. I. Liechtenstein, V. I. Anisimov and J. Zaanen, *Phys. Rev. B: Condens. Matter Mater. Phys.*, 1995, **52**, R5467.
- 32 S. L. Dudarev, G. A. Botton, S. Y. Savrasov, C. J. Humphreys and A. P. Sutton, *Phys. Rev. B: Condens. Matter Mater. Phys.*, 1998, **57**, 1505.
- 33 N. C. Hernández, R. Grau-Crespo, N. H. de Leeuw and J. F. Sanz, *Phys. Chem. Chem. Phys.*, 2009, **11**, 5246.
- 34 J. Hong, A. Stroppa, J. Íñiguez, S. Picozzi and D. Vanderbilt, *Phys. Rev. B: Condens. Matter Mater. Phys.*, 2012, **85**, 054417.
- 35 P. Rivero, V. Meunier and W. Shelton, *Phys. Rev. B: Condens. Matter Mater. Phys.*, 2016, **93**, 024111.
- 36 J. P. Perdew, K. Burke and M. Ernzerhof, *Phys. Rev. Lett.*, 1996, **77**, 3865.
- 37 G. Kresse and J. Fürthmüller, *Phys. Rev. B: Condens. Matter Mater. Phys.*, 1996, **54**, 11169; G. Kresse and D. Joubert, *Phys. Rev. B: Condens. Matter Mater. Phys.*, 1999, **59**, 1758.
- 38 D. M. Ceperley and B. J. Alder, *Phys. Rev. Lett.*, 1980, **45**, 566.
- 39 J. P. Perdew, A. Ruzsinszky, G. I. Csonka, O. A. Vydrov, G. E. Scuseria, L. A. Constantin, X. Zhou and K. Burke, *Phys. Rev. Lett.*, 2008, **100**, 136406.
- 40 P. E. Blöchl, *Phys. Rev. B: Condens. Matter Mater. Phys.*, 1994, **50**, 17953.
- 41 C. Cazorla and J. Boronat, *Phys. Rev. B: Condens. Matter Mater. Phys.*, 2015, **92**, 224113.
- 42 G. Kresse, J. Furthmüller and J. Hafner, *Europhys. Lett.*, 1995, **32**, 729.
- 43 D. Alfè, G. D. Price and M. J. Gillan, *Phys. Rev. B: Condens. Matter Mater. Phys.*, 2001, **64**, 045123.
- 44 D. Alfè, *Comput. Phys. Commun.*, 2009, **180**, 2622.
- 45 R. Dovesi, R. Orlando, A. Erba, C. M. Zicovich-Wilson, B. Civalleri, S. Casassa, L. Maschio, M. Ferrabone, M. De La Pierre, P. D'Arco, Y. Noel, M. Causa, M. Rerat and B. Kirtman, *Int. J. Quantum Chem.*, 2014, **114**, 1287.
- 46 <http://www.crystal.unito.it/basis-sets.php>.
- 47 P. J. Hay and W. R. Wadt, *J. Chem. Phys.*, 1985, **82**, 299.
- 48 S. Piskunov, E. Heifets, R. I. Eglitis and G. Borstel, *Comput. Mater. Sci.*, 2004, **29**, 165.
- 49 F. Corà, *Mol. Phys.*, 2005, **103**, 2483.
- 50 C. Adamo and V. Barone, *J. Chem. Phys.*, 1999, **110**, 6158.
- 51 A. V. Krukau, O. A. Vydrov, A. F. Izmaylov and G. E. Scuseria, *J. Chem. Phys.*, 2006, **125**, 224106.
- 52 X. Huang, C. Bungaro, V. Godlevsky and K. M. Rabe, *Phys. Rev. B: Condens. Matter Mater. Phys.*, 2001, **65**, 014108.
- 53 C. Cazorla, D. Alfè and M. J. Gillan, *Phys. Rev. B: Condens. Matter Mater. Phys.*, 2012, **85**, 064113.
- 54 D. Andrault and J. P. Poirier, *Phys. Chem. Miner.*, 1991, **18**, 91.
- 55 J. Íñiguez and D. Vanderbilt, *Phys. Rev. Lett.*, 2002, **89**, 115503.
- 56 J.-Y. Yang, M. Medarde, J. S. White, D. Sheptyakov, X.-Z. Yan, N.-N. Li, W.-G. Yang, H.-L. Xia, J.-H. Dai, Y.-Y. Yin, Y.-Y. Jiao, J.-G. Cheng, Y.-L. Bu, Q.-F. Zhang, X.-D. Li, C.-Q. Jin, Y. Taguchi, Y. Tokura and Y.-W. Long, *Phys. Rev. B: Condens. Matter Mater. Phys.*, 2015, **92**, 195147.
- 57 J. Íñiguez, *Phys. Rev. Lett.*, 2008, **101**, 117201.
- 58 J. C. Wojdeł and J. Íñiguez, *Phys. Rev. Lett.*, 2010, **105**, 037208.
- 59 O. Diéguez, O. E. González-Vázquez, J. C. Wojdeł and J. Íñiguez, *Phys. Rev. B: Condens. Matter Mater. Phys.*, 2011, **83**, 094105.
- 60 C. Cazorla and M. Stengel, *Phys. Rev. B: Condens. Matter Mater. Phys.*, 2015, **92**, 214108.